Local axisymmetry-breaking–induced transition of trapped-particle orbit and loss channels in quasi-axisymmetric stellarators

Lang Yang[1], Haifeng Liu[1,4(a)], Akihiro Shimizu[2], Yuhong Xu[1], Xianqu Wang[1], Hai Liu[1], Changjian Tang[1,3], Yangbo Li[1], Jinmao Liu[1], Yang Luo[1], Guozhen Xiong[1], Chunyan Su[4], Shigeyoshi Kinoshita[2], Mitsutaka Isobe[2,3], Shoichi Okamura[2], Jie Huang[1], Xin Zhang[1], Dapeng Yin[5], Yi Wan[5] and CFQS team[1,2,5]

[1] *Institute of Fusion Science, School of Physical Science and Technology, Southwest Jiaotong University Chengdu 610031, China*
[2] *National Institute for Fusion Science, National Institutes of Natural Sciences - Toki 509-5292, Japan*
[3] *The Graduate University for Advanced Study, SOKENDAI - Toki 509-5292, Japan*
[4] *College of Physics, Sichuan University - Chengdu 610065, China*
[5] *Hefei Keye Electro Physical Equipment Manufacturing Co., Ltd. - Hefei 230000, China*

Abstract – The transition of trapped-particle orbit topologies has been investigated in quasi-axisymmetric (QA) configurations, such as the Chinese First Quasi-axisymmetric Stellarator (CFQS). It is found that the axisymmetry-breaking phenomenon in QA configurations is of great significance at some specific locations, which could easily induce blocked particles to transit into localized particles. A novel aspect is presented to interpret the transition mechanism of trapped-particle orbit topologies in this paper, *i.e.*, as the amplitudes of non-axisymmetric field increase along the radius direction, the region of large toroidal inhomogeneity is gradually generated, which makes the length of the trapped-particle trajectory substantially short, and hence, may restrict particles to a single helical field period. Meanwhile, at such locations the "pseudo-axisymmetric" field results in coupling of the maximum radial drift and the minimum poloidal drift, which enables the transition of trapped-particle orbit topologies considerably and forms specific loss channels, degrading plasma confinement. These results may shed light on the optimization of QA configurations via avoidance of such coupling with respect to energetic particle confinement. Moreover, this work is also relevant to the generation of inhomogeneity of particle flux deposition on the devertor plates.

Introduction. – In the fusion devices the axisymmetry breaking and three-dimensional (3D) effects grow more and more interesting and important [1]. In a tokamak a three-dimensional configuration generated by resonant magnetic perturbation coils could mitigate the edge localized modes [2]; in the optimization of stellarator configurations [3], plasma confinement and MHD stability could be enhanced via suppression of large non-symmetric components [4]; in the reversal field pinch self-organization driven by a single helical equilibrium with a 3D magnetic topology reduces the magnetic fluctuations, resulting in the onset of a transport barrier [5].

As a subclass of omnigenity, the QA configuration [6] is particularly interesting, as it can be thought of as a generalization of axisymmetry. Similarly to tokamaks, QA equilibria possess a magnetic field strength that is nearly symmetric in the toroidal Boozer coordinate. They thus share many neoclassical properties with tokamaks. These configurations are capable of being compact due to their relatively large bootstrap current which provides a source of rotational transform, in addition to that from the coils. On the other hand, the similarity to stellarators provides

potential benefits: QA configurations can run in a steady state potentially without any plasma current drive, avoiding MHD disruptions. However, in fact it is generally not possible to achieve axisymmetric features across the entire volume on behalf of keeping a sufficient amount of freedom in the configuration solutions [7]. This paper is focused on the significant axisymmetry-breaking phenomenon on the QA configurations to distinguish at which specific locations serious pseudo-symmetry takes place and how to drive the transition of trapped-particle orbit topologies to form loss channels.

Generally, in an axisymmetric geometry, two kinds of trajectories may be produced by the shape of trajectories projected on the cross-section [8]: the circle-shaped orbits for passing particles and banana-like orbits for trapped particles in axisymmetric tokamaks. In QA configurations there are toroidal ripple (dominant one) and non-axisymmetric ripples. The toroidal ripple is similar to that in tokamaks and the non-axisymmetric ripples mainly contains bumpy ripples and helical ripples which could induce the axisymmetry breaking phenomena. These two kinds of ripples can cause localized particles and the blocked particles respectively, which are interpreted as follows [9–11].

Localized particle: localized particles which are trapped within a single helical field period would remain locally and can never travel to the next helical field period.

Blocked particle: blocked particles' trajectories are not restricted to a single helical field period due to the slowly variational toroidal ripple but extend to neighboring helical field periods. However, they do not pass completely round the minor cross-section, which are toroidally bounded by two isosurfaces, $B = B_{\text{ref}}$ (B_{ref} represents the magnetic field strength at the bounce point). These motions of particles are simultaneously affected by toroidal ripple and non-axisymmetric ripples. Therefore, the distinction of types of trapped particles is primarily determined by which kind of ripples have a more pronounced effect. It implies that the transition of trapped-particle orbits can come up by the spatial variation of the dominant ripple in QA configurations.

In this paper the CFQS configuration is mainly utilized for revealing the transition mechanism of trapped-particle orbit topologies and generation of loss channels. The CFQS is a joint project of international collaboration. It is designed and fabricated by the Southwest Jiaotong University (SWJTU) in China and the National Institute for Fusion Science (NIFS) in Japan [12]. The equilibrium calculation has been performed with the VMEC code [13].

The distinction between axisymmetric and QA configurations. – The plasma geometry is defined by the shape of a constant pressure surface near the edge of the plasma. In (R, φ, Z) cylindrical coordinates, R and Z have no dependence on the toroidal angle in the axisymmetric configuration. The shape of poloidal cross-sections is conventionally expressed as

$$R(\theta) = R_0 + a\cos(\theta + \delta\sin\theta), \quad (1)$$
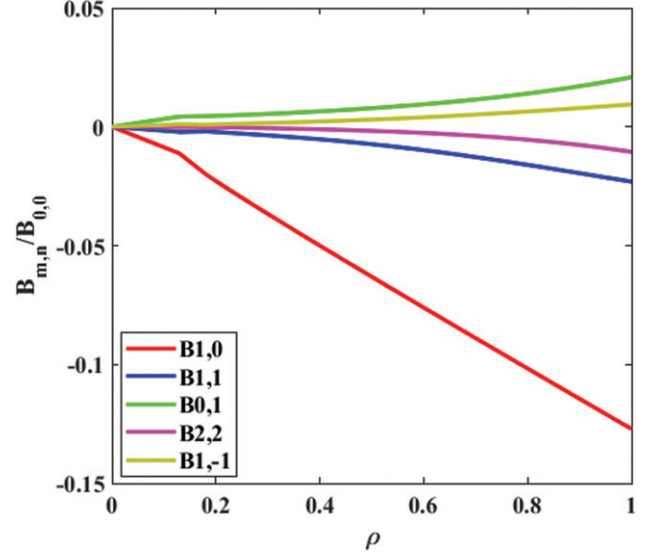

Fig. 1: Magnetic field strength spectrum in Boozer coordinates for a vacuum case without $B_{0,0}$ in the CFQS. The normalized radius $\rho = \sqrt{\frac{\psi}{\psi_{LCFS}}}$.

$$Z(\theta) = \kappa a\sin\theta, \quad (2)$$

where R_0 is the major radius, a is the minor radius or half-width of the plasma, κ is the elongation and δ is the triangularity [1]. Similarly, the magnetic field strength is just dependent on the θ and R.

In stellarators a standard expression for the plasma boundary is the Garabedian representation which is described in cylindrical coordinates by the Fourier decomposition as follows [14]:

$$R = \sum_{m,n} R_{mn}(\psi)\cos(m\theta - nN\zeta), \quad (3)$$

$$Z = \sum_{m,n} Z_{mn}(\psi)\sin(m\theta - nN\zeta), \quad (4)$$

$$\phi = \zeta, \quad (5)$$

where θ and ζ are mathematic poloidal angle and toroidal angle, ψ represents the magnetic flux. R and Z are dependent on the toroidal angle and form a three-dimensional non-axisymmetric geometry which is utterly different from the tokamak. The 3D magnetic field strength can be expanded in Boozer coordinates with a form of Fourier series:

$$B(\psi, \theta_B, \phi_B) = \sum_{m,n}(B_{mn}(\psi)\cos(m\theta_B - nN\phi_B)). \quad (6)$$

The coefficients B_{mn} are referred to as the spectrum of the magnetic field strength. The ψ, θ_B and ϕ_B form the spatial Boozer coordinates. The quasi-axisymmetry means that only the first row of coefficients $B_{m,0}$ is large enough to matter, as in tokamaks. The ordinary differential equations for guiding center orbits show that good neoclassical transport will prevail in the quasi-axisymmetric configurations [15,16].
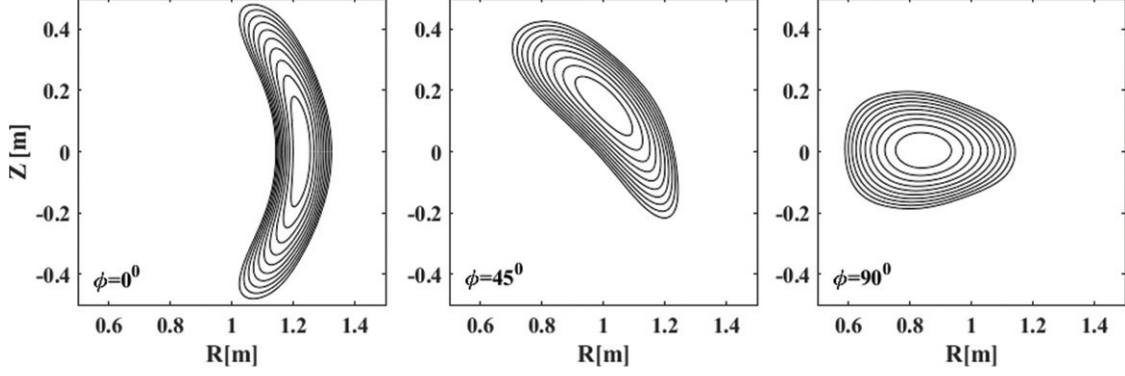
Fig. 2: Poloidal cross-sections of magnetic flux surfaces in the CFQS equilibrium calculated by VMEC code.

Figure 1 depicts the spectrum of the magnetic field strength in the CFQS configuration. The magnetic field strength is $1.0\,\mathrm{T}$. To distinguish the small-amplitude components, the largest component $B_{0,0}$ is omitted and the other components are normalized by $B_{0,0}$. The non-axisymmetric ripples consist of a bumpy ripple ($B_{0,1}$) and helical ripples ($B_{1,1}$, $B_{2,2}$, $B_{1,-1}$, etc.) from the magnetic field strength spectrum. These non-axisymmetric ripples are much less than $B_{1,0}$, which indicates a tokamak-like or quasi-axisymmetric configuration.

Figure 2 displays three poloidal cross-sections of the magnetic flux surfaces for the plasma pressure-free case. These magnetic flux surfaces indicate large axisymmetric (or toroidal average) crescent, elongation and triangularity, which enhance the stability of ballooning and kink modes. On the other hand, the spatial variation of non-axisymmetric ripples can cause the differences of cross-section shapes along the toroidal precession in the CFQS configuration, which can give rise to existence of locally maximum axisymmetry breaking. It plays an important role on the transition of particle orbit topologies which will be illustrated as follows.

Transition of trapped particles in the CFQS. – Figure 3 shows the contour of mJ on the (ρ, ζ_N)-plane in the CFQS configuration. J is the second adiabatic invariant $J = \int v_{\parallel}\,\mathrm{d}l$ and m is the mass of the trace particle. The normalized poloidal angle $\theta_N = \theta/(2\pi/N)$ and the toroidal angle $\zeta_N = \zeta/(2\pi/N)$. Input parameters $B_{\mathrm{ref}} = 0.95\,\mathrm{T}$ and traced particle energy is $0.01\,\mathrm{keV}$. Such low particle energy could lead the trapped-particle orbit to rest on a magnetic flux surface without significant deviation from that surface. It is beneficial to the calculation of J [17,18]. In fig. 3 a "singular" characteristic is observed, that is the value of J decreases rapidly at the "blue" points A. It indicates the loss of length of particle orbit is of significance there. In stellarators, the trapped particles encounter transitioning regions and their orbital type is changed and radial drift may cause them to escape the last closed flux surface (LCFS) before detrapping occurs. It indicates that at these specific regions loss channels exist where particles could fall in and transit into outward
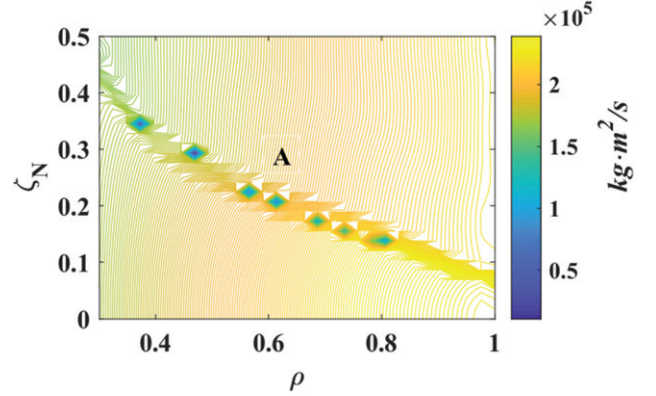

Fig. 3: The contour mJ on the (ρ, ζ_N)-plane in the CFQS.

drifted localized particles in QA configurations. In the next section, we will investigate what physical mechanism induces such an orbital transition and loss channels.

Transition mechanism of trapped-particle orbit topologies. – One reason for the transition of the trapped-particle orbit (blocked particles convert to localized particles) may arise from the length loss of the trajectory. In order to find what parameters make the trajectory short, the evolution of $v_{\parallel}$ of test particles along trajectories is examined. Figure 4(a) shows the variation of $v_{\parallel}$ as a function of time along a trajectory. Input parameters $B_{\mathrm{ref}} = 0.95\,\mathrm{T}$ and the particle energy is $0.01\,\mathrm{keV}$. The area below the $v_{\parallel}$ curve corresponds to the length of the particle orbit l because $\mathrm{d}l$ can be expressed as $\mathrm{d}l = v_{\parallel}\mathrm{d}t$ on account of the low energy of the trapped particle. Due to its periodicity, only a quarter of the banana orbit is displayed. The ratio of the length of each trajectory from $\zeta_N = 0.5$ on $\rho = 0.35$, 0.6 and 0.95 is about 1:0.88:0.75. The difference of initial $v_{\parallel}$ is dependent on the difference of B at initial points. Figure 4(b) shows the contours of the toroidal inhomogeneity of B, $\lambda \equiv (1/B)/(\partial B/\partial \zeta)$, on the magnetic surfaces ($-1 \leqq \theta_N \leqq 1$ and $0 \leqq \zeta_N \leqq 2$) at the three radii. The trajectories (bold straight lines) of particles launched from $\zeta_N = 0$ and 0.5 on each surface are also depicted. The contours of $\lambda = 0$ are represented by dashed curves and the interval of contours is 1%. The
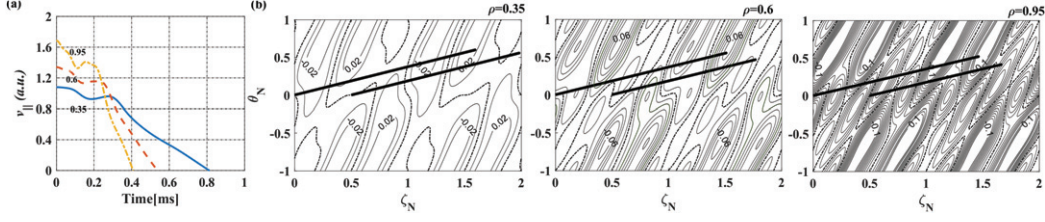
Fig. 4: (a) The time evolution of $v_{\parallel}$ of tracer particles launched from $\zeta_N = 0.5$ on $\rho = 0.35$ (blue), 0.6 (red) and 0.95 (yellow). (b) Contours of $\lambda = \frac{1}{B}\frac{\partial B}{\partial \zeta}$ on the (ζ_N, θ_N)-plane at $\rho = 0.35$, 0.6 and 0.95. Trajectories of tracer particles launched from $\zeta_N = 0$ and 0.5 are also shown by bold straight lines.
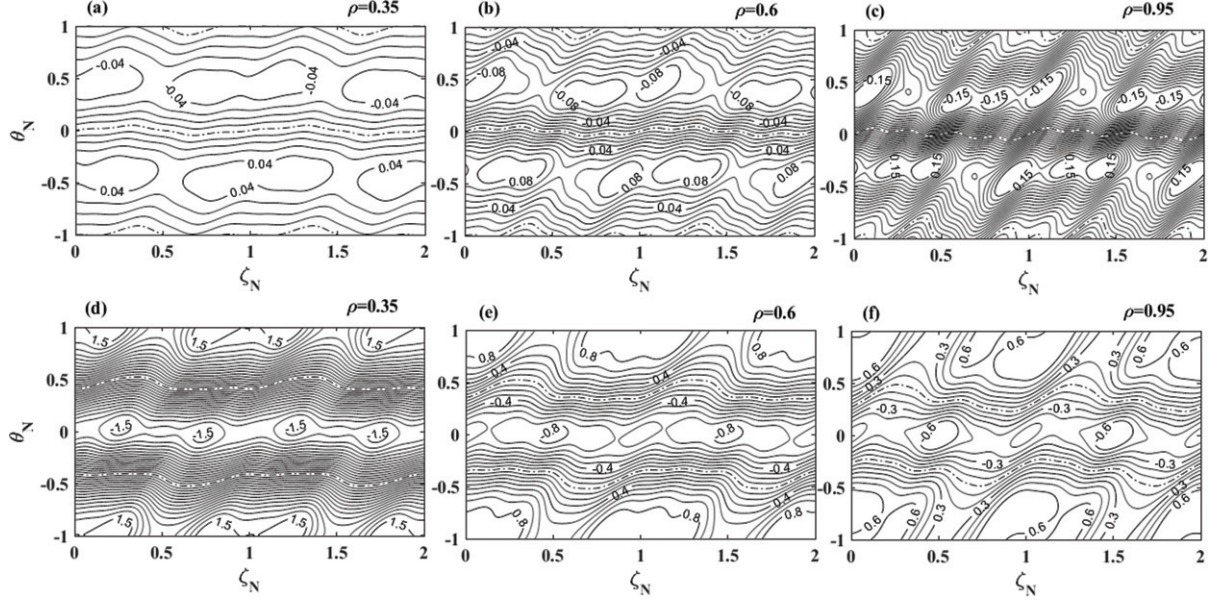

Fig. 5: The contour of radial drift ((a)–(c)) and poloidal drift ((d)–(f)) on the three flux surfaces with $\rho = 0.35$, 0.6 and 0.95 for a vacuum field case in the CFQS.

maximum and minimum strength of the inhomogeneity are labeled in fig. 4(b). The coupling of toroidal ripple and non-axisymmetric ripples are more evident when $\rho \geqq 0.6$ and $\lambda \geqq 6\%$. The region with $\lambda < 0$ ($\lambda > 0$) shows that B decreases (increases) as ρ is increased. This contour plot is greatly beneficial to interpret the contribution from toroidal inhomogeneity of B to the variation of $v_{\parallel}$. It shows that the non-axisymmetry of B is enhanced as ρ is increased. In the angular phase-space domain where $\cos(\theta - N\zeta) = -\cos(N\zeta)$, the $B_{1,1}$ and $B_{0,1}$ components of B interfere constructively, causing their contribution to B to become significant (because $B_{1,1} < 0$ and $B_{0,1} > 0$ as shown in fig. 1), which gives rise to a localized region with enhanced λ as seen in fig. 4(b). Notably the toroidal inhomogeneity $\lambda \geqq 6\%$ could cause the $v_{\parallel}$ to decrease efficiently as the particles launched from $\zeta_N = 0.5$ pass this region in fig. 4(b). This is more obvious for the outer radius and the length of trajectories of the trapped particle becomes smaller compared to that of the inner radius by a large reduction in $v_{\parallel}$. The particle launched from $\zeta_N = 0$ is similar to the former. This aspect is a novel feature to interpret the transition of trapped particles at the outer radius.

The other factor for the transition of blocked particles could result from particle drift motions in QA configurations. Figure 5 shows the topography of radial drift ((a)–(c)) and poloidal drift ((d)–(f)) at three radii, where the normalized radius ρ are 0.35, 0.6 and 0.95, respectively ($-1 \leqq \theta_N \leqq 1$ and $0 \leqq \zeta_N \leqq 2$). The spectrum of B in the CFQS configuration is given in fig. 1. The two formulas $-\frac{1}{B}\frac{\partial B}{\partial \theta}(\frac{1}{B}\frac{\partial B}{\partial \psi})$ are examined to evaluate radial (poloidal) drift [19,20]. The radial drift is outwards for the region where the contours have positive values. Particles which remain in the region with positive values will finally reach the plasma boundary. On the contrary, if particles remained in the region with negative values will drift inward. This paper is focused on the region with positive values.

Figure 5(a)–(c) shows the contours of the radial drift, $\alpha_{dr} = -\frac{1}{B}\frac{\partial B}{\partial \psi}$ on magnetic surfaces at these three radii in the CFQS. The contours of $\alpha_{dr} = 0$ are plotted by dashed curves and the interval of contours is 1%. It is worth noting that at some specific locations, θ near $-\pi/2$, the positive maximum of α_{dr} appears and the magnitude of α_{dr} increases with increasing the normalized radius. Figure 5(d)–(f) depicts the contours of the poloidal drift,
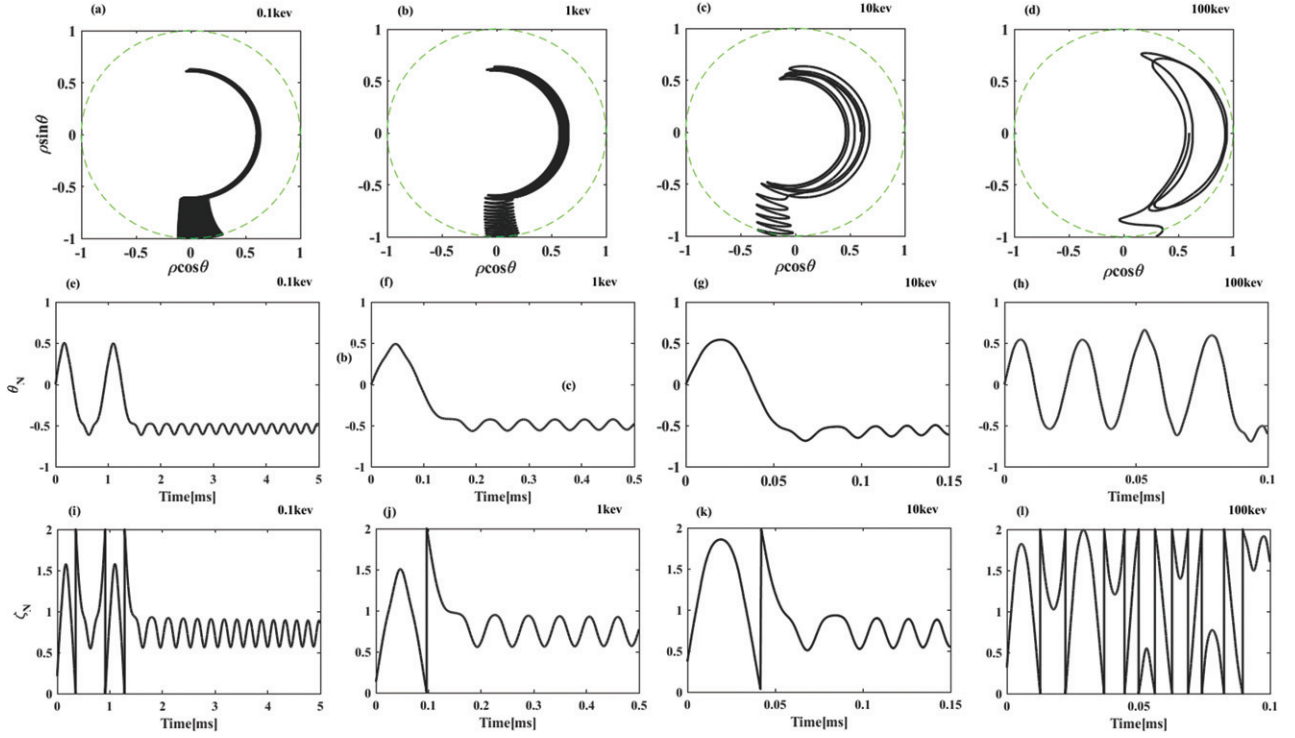
Fig. 6: Orbit topologies of transition particle with various particle kinetic energies: (a) for 0.1 keV, (b) for 1 keV, (c) for 10 keV, (d) for 100 keV. (e)–(h): the normalized poloidal position evolution of transition particle. (i)–(l): the toroidal position evolution of transition particle.

$\beta_{d\theta} = \frac{1}{B}\frac{\partial B}{\partial \psi}$ on magnetic flux surfaces. The contours of $\beta_{d\theta} = 0$ are also shown by dashed curves and the interval of contours is 10%. The value of $\beta_{d\theta}$ decreases as the normalized radius increases. The strength of the poloidal drift ((d)–(f)) is much stronger than the strength of radial drift ((a)–(c)) in fig. 5. Thus, the QA configurations have good confinement properties for collisionless particles. However, at some regions the minimum $\beta_{d\theta}$ turns up close to where the maximum α_{dr} exists, which could shorten the length of particle trajectories and could induce blocked particles to convert into localized ones more easily. In addition, this coupling regions indicate loss channels where particles fall in and escape the last closed flux surface (LCFS). These coupling regions of the maximum radial drift and the minimum poloidal drift come up at θ near $-\pi/2$ and ζ near π or 2π. The coupling between maximum radial drift and minimum poloidal drift is caused by locally significant symmetry-breaking fields. In the CFQS, the first two dominant components of B are $B_{1,0}$ and $B_{1,1}$, whose spatial variation could be expressed by the following equations:

$$\hat{B}_{1,0} = B_{1,0}\cos(\theta), \qquad (7)$$

$$\hat{B}_{1,1} = B_{1,1}\cos(\theta - N\zeta). \qquad (8)$$

The component $B_{1,0}$ is much larger than other components and almost determines the distribution of the magnetic field strength along the poloidal direction. Therefore, the poloidal drift is highly dependent on it because of

$\beta_{d\theta} = \frac{1}{B}\frac{\partial B}{\partial \psi} \propto B_{1,0}\cos(\theta)$. Therefore, the minimum poloidal drift ($\beta_{d\theta} = 0$) comes up when $\theta = -\frac{\pi}{2}$ or $\frac{\pi}{2}$, which is in agreement with the simulation results shown in fig. 6(d)–(f). In addition, the radial drift is attributed to the conjunct contribution from $\hat{B}_{1,0}$ and $\hat{B}_{1,1}$, i.e., $\alpha_{dr} = -\frac{1}{B}\frac{\partial B}{\partial \theta} \propto B_{1,0}\sin(\theta) + B_{1,1}\sin(\theta - 2\zeta)$ ($N = 2$ in CFQS). Thus, $\sin(\theta) = \sin(\theta - 2\zeta) = -1$ can maximize the outward radial drift. In other words, when $\theta = -\pi/2$ and $\zeta = \pi$, 2π the maximum radial drift takes place, which is consistent with the results given in fig. 6(a)–(c). Therefore, at $\theta = -\pi/2$ and $\zeta = \pi$ and 2π loss channels exist where particles could fall in and transit into outward-drifted localized particles in the CFQS configuration.

Figure 6 displays transition of trapped-particle orbit topologies with various particle kinetic energies. The simulated particles are hydrogen ions with 0.1 keV, 1 keV, 10 keV and 100 keV, respectively, in fig. 6(a)–(d), whose initial spatial positions are located at point A in fig. 3. The traced particles are able to change their orbit class (from blocked particles to localized ones) when their non-adiabatic properties are largely changed. It is also depicted, in fig. 3, that the J value at blue points decreases rapidly. In that case trapped particles fall into specific loss channels where the maximum radial drift and the minimum poloidal drift come up simultaneously. Figures 6(e)–(h) and (i)–(l) show normalized poloidal position and toroidal position of transited particle over time, respectively. They show that the transition regions of
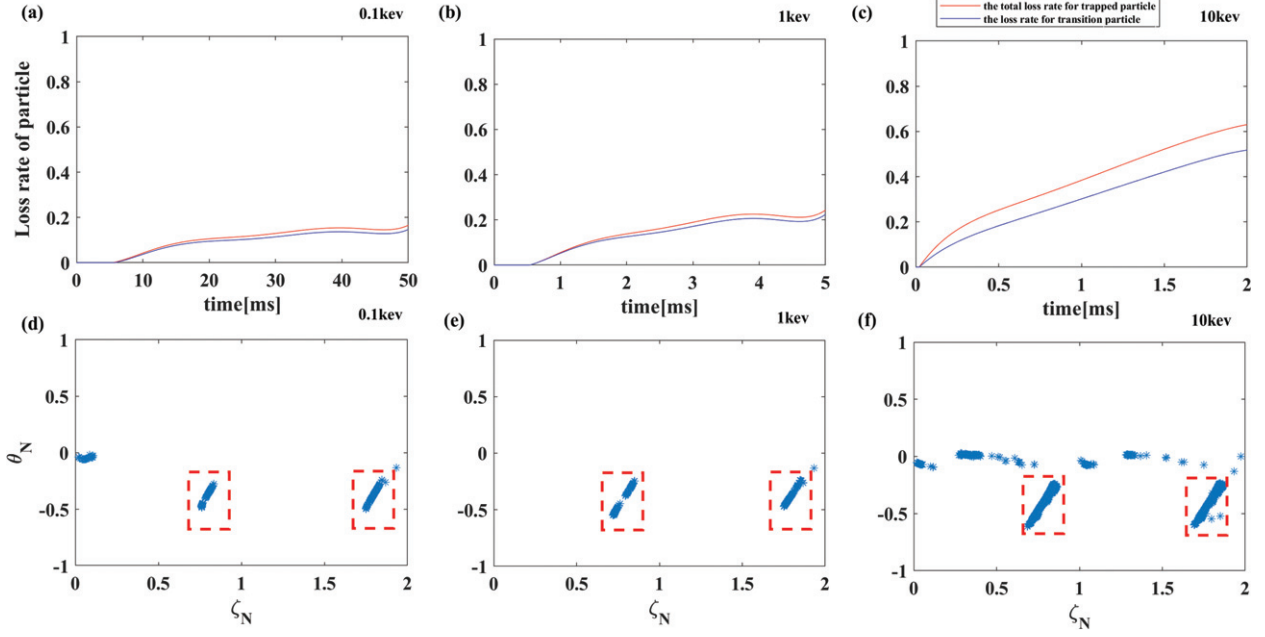
Fig. 7: The loss rate evolution of trapped particles in the CFQS: (a) for 0.1 keV, (b) for 1 keV and (c) for 10 keV. The red curve represents the total loss rate evolution of trapped particles. The blue curve represents the loss rate evolution of the transition particles from blocked particles to localized ones. (d)–(f): lost particle position in the (θ_N, ζ_N)-plane, the red dashed rectangles represent specific loss channels by transition particles.
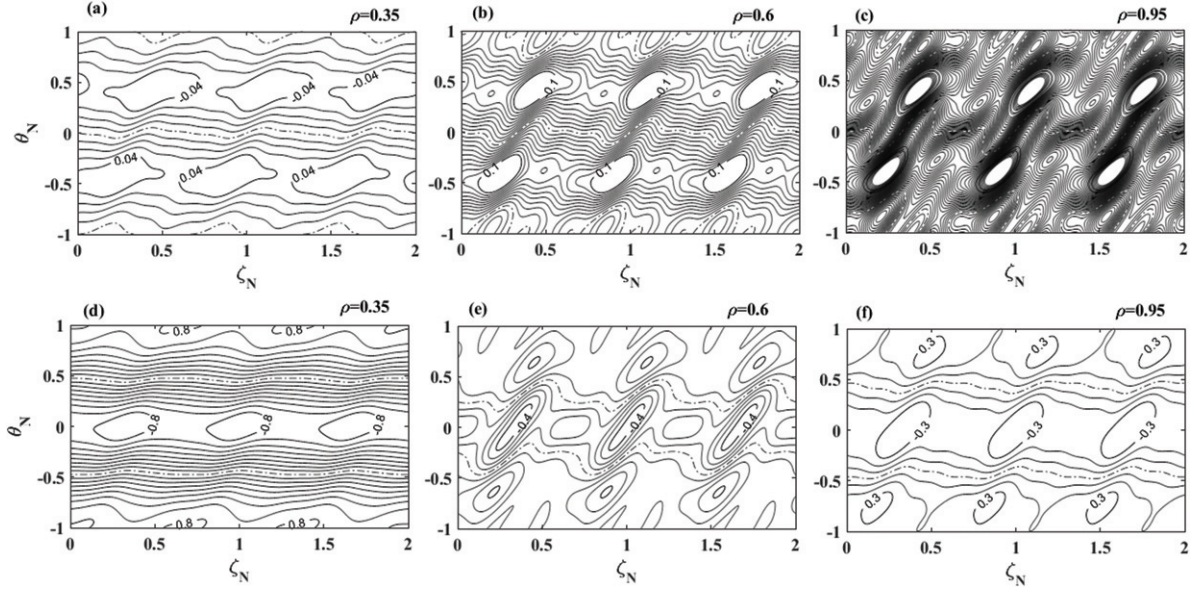

Fig. 8: The contour of radial drift ((a)–(c)) and poloidal drift ((b), (e), (f)) on the three flux surfaces with $\rho = 0.35$, 0.6 and 0.95 in a NCSX-like configuration.

trapped particles correspond exactly to the predicted overlapping regions, where θ near $-\pi/2$ ($\theta_N \approx -0.5$) and ζ near π and 2π ($\zeta_N \approx 1$ or 2). In other words, there are two loss channels caused by transition particles in the CFQS configuration.

Figure 7(a)–(c) shows the loss rate of trapped particles in the CFQS configuration at the outer radius ($\rho = 0.7$). In each simulation 2000 mono-energetic particles with 0.1 keV, 1 keV, and 10 keV are initially located at $\rho = 0.7$, $\theta_N = 0$ and $\zeta_N = 0$. Pitch angles of particles almost cover the entire trapped-particle region from $70°$ to $110°$. The red curve represents the total loss rate evolution of trapped particles. The blue curve represents the loss rate evolution of the transition particles from the blocked ones converting to localized ones. It is shown that the loss rate caused by transition particles accounts for more than 70%

of lost trapped particles. Figure 7(d)–(f) shows locations of the loss particles in the (θ_N, ζ_N)-plane. The red dashed rectangles emphasize the coupling regions (loss channels) of the maximum radial drift and the minimum poloidal drift, where θ_N is around -0.5 and ζ_N is close to 1 and 2. It shows that most trapped particles are lost from these specific loss channels. These loss channels are in great agreement with what is illustrated in fig. 5 and with analytic predictions of eqs. (7) and (8). This feature is unique in QA stellarators. Moreover, as the particle energy increases, the loss rate is increased.

The phenomenon of the trapped-particle trajectory transition has been observed in the CFQS configuration with $N = 2$. It would be highly necessary to examine whether in other QA categories the special loss channels for the transition of trapped particles are generated or not. Thus, the other QA configuration with $N = 3$, National Compact Stellarator Experiment (NCSX)-like configuration (major radius $R = 1\,\mathrm{m}$, $Ap = 4.4$), is also taken into account [21]. Figure 8 shows the topography of radial drift ((a)–(c)) and poloidal drift ((d)–(f)) at three radii, $\rho = 0.35$, 0.6 and 0.95, respectively. Similarly, at $\theta_N \approx -0.5$, the overlapping of maximum radial drift and minimum poloidal drift also appears. The difference is that, in this configuration, there are three toroidal regions with maximum radial and minimum poloidal drifts $\zeta_N \approx 0.2$, 0.8 and 1.5, arising from toroidal periodic number $N = 3$. In other words, the dominant non-axisymmetric component in the NCSX configuration is different from that in the CFQS, which mainly determines the toroidal positions of trapped-particle orbit transition. It may be predicted that the transition of trapped particles in the QAs with high N is more considerable than that in the QAs with low N when other conditions/parameters are fixed.

Summary. – The transition of trapped-particle orbit topologies driven by symmetry-breaking fields has been investigated systemically in the CFQS configuration. The helicity $B_{1,1}$ and bumpy field $B_{0,1}$ mainly give rise to the toroidal inhomogeneity of the magnetic field globally on magnetic flux surfaces. As the amplitude of helicity and bumpy field increase the region of toroidal inhomogeneity with $\lambda \geqq 6\%$ is gradually hatched at outer radius ($\rho = 0.6$–1). In this region, the length of a trapped-particle trajectory is lost substantially, which is capable to restrict particles to a single helical field period.

Meanwhile, the enhancement of the radial drift and wakening of the poloidal drift arise as the radius increases. On a magnetic flux surface variation of toroidicity $B_{1,0}$ and helicity $B_{1,1}$ cause the coupling between the maximum radial drift and the minimum poloidal drift. This coupling can make the length of trapped-particle trajectories dramatically short, which enhances the transition from blocked particles to localized particles. These particles located in such regions drift radially outwards and eventually escape the last closed flux surface. The

same phenomenon is also observed in the NCSX-like configuration.

Above all, the voidance of such coupling (loss channels) would mitigate this drift-induced trapped-particle orbit transition and should be taken in account as an additional strategy to optimize stellarators with respect to energetic particle orbit confinement. Concerning the CFQS, auxiliary trim coils might be considered to mitigation of such transition.

REFERENCES

[1] BOOZER A. H. *et al.*, *Phys. Plasmas*, **16** (2009) 058102.
[2] LORENZINI R. *et al.*, *Nat. Phys.*, **5** (2009) 570.
[3] HELANDER P *et al.*, *Plasma Phys. Control. Fusion*, **51** (2009) 124009.
[4] BOOZER A. H. *et al.*, *Nucl. Fusion*, **55** (2015) 25001.
[5] XU Y. *et al.*, *Matter Radiat. Extrem.*, **1** (2016) 192.
[6] NÜHRENBERG J., LOTZ W. and GORI S., *Quasi-axisymmetric tokamaks*, in *Theory of Fusion Plasmas* (Editrice Compositori, Bologna) 1994, p. 3.
[7] GARREN D. A. and BOOZER A. H., *Phys. Fluids*, **3** (1991) 2822.
[8] LIN J. B., ZHANG W. L., LIU P. F. *et al.*, *Chin. Phys. Lett.*, **35** (2018) 025201.
[9] WAKATANI MASAHIRO, *Stellarator and Heliotron Devices,* in *International Series of Monographs on Physics*, Vol. **95** (Oxford University Press, New York, Oxford) 1998, p. 229.
[10] GIBSON A. and TAYLOR J. B., *Phys. Fluids*, **10** (1967) 2653.
[11] FAUSTIN J. M., COOPER W. A. *et al.*, *Nucl. Fusion*, **56** (2016) 092006.
[12] XU Y. *et al.*, *27th IAEA Fusion Energy Conference* (IAEA) 2018.
[13] HIRSHMAN S. P. *et al.*, *Comput. Phys. Commun.*, **43** (1986) 143.
[14] BAUER F., BETANCOURT O. and GARABEDIAN P. (Editors), *Magnetohydrodynamic Equilibrium and Stability of Stellarators* (Springer-Verlag, New York) 1984, p. 225.
[15] AKIHIRO S. *et al.*, *Plasma Fusion Res.*, **13** (2018) 3403123.
[16] HAIFENG L. *et al.*, *Plasma Fusion Res.*, **13** (2018) 3405067.
[17] HASTIE R. J., TAYLOR J. B., HAAS F. A. *et al.*, *Ann. Phys.*, **41** (1967) 302.
[18] MASAYUKI Y., KIMITAKA I., SHOICHI O. *et al.*, *Nucl. Fusion*, **42** (2002) 1094.
[19] YOKOYAMA M. *et al.*, *Nucl. Fusion*, **41** (2001) 215.
[20] YOKOYAMA M. *et al.*, *Nucl. Fusion*, **40** (2000) 2.
[21] ZARNSTORFF M. C., BERRY L. A., BROOKS A. *et al.*, *Plasma Phys. Control. Fusion*, **43** (2001) A237.